# Quantum oscillations in an excitonic insulating electron-hole bilayer

Yuelin Shao [1,2,*] and Xi Dai[3,†]

[1]*Beijing National Laboratory for Condensed Matter Physics and Institute of Physics, Chinese Academy of Sciences, Beijing 100190, China*
[2]*School of Physical Sciences, University of Chinese Academy of Sciences, Beijing 100049, China*
[3]*Department of Physics, The Hongkong University of Science and Technology, Clear Water Bay, Kowloon 999077, Hong Kong, China*

(Received 4 January 2024; revised 28 February 2024; accepted 20 March 2024; published 2 April 2024)

We study the quantum oscillations of interlayer capacitance in an excitonic insulating electron-hole double layer with the Hartree-Fock mean-field theory. Such oscillations could be simply understood from the physical picture of an exciton formed by electron and hole Landau levels, in which the direct gap between the electron-hole Landau levels will oscillate with the exciton chemical potential and the inverse of the magnetic field. We also find that the excitonic order parameters can be destroyed by a strong magnetic field. At this time, the system becomes two independent quantum Hall liquids, and the interlayer capacitance oscillates to zero at zero temperature.

DOI: 10.1103/PhysRevB.109.155107

## I. INTRODUCTION

A two-dimensional bilayer separated by a perfect insulating barrier is expected to be a candidate system for realizing exciton condensation and the excitonic insulator (EI) phase at the charge neutrality point (CNP), where the two layers are equally charged by electrons and holes [1–11]. Evidence of the EI phase in such a bilayer was first observed in quantum well system [12] and was also identified in dual-gated transition metal dichalcogenide (TMD) double layers recently [13–16]. In this paper, we focus on the TMDs bilayer, and the experimental setup is illustrated in Fig. 1(a), where the electron layer (blue) and hole layer (orange) are sandwiched between the top and bottom gates (black) and dielectric spacers (gray) are inserted between gates and layers to avoid direct tunneling. The gate-layer voltage $(V_e + V_h)/2$ is used to control the overall chemical potential $\mu$ to make the system charge neutral. And the exciton density (charge number density per layer) $n_{ex}$ is tuned by the exciton chemical potential $\mu_{\rm ex} = eV_b - E_g$, where $V_b = V_h - V_e$ is the interlayer bias voltage and $E_g$ is the spatially indirect gap between the electron and hole bands at zero bias.

Low-energy excitations of single-layer TMDs near the valley center are approximated as free fermions with quadratic dispersion [17]. By tuning the exciton chemical potential $\mu_{\rm ex}$, a typical noninteracting band structure at the CNP is illustrated in Fig. 1(b), where the electron and hole layers have nested Fermi surfaces. In the absence of single-particle tunneling $t$, the electron and hole layers have separate charge conservations, and the system has a $\mathrm{U}_e(1) \times \mathrm{U}_h(1)$ symmetry. However, when interlayer excitons are generated and condensed due to the attractive interaction between electrons and holes, a nonzero mean-field interlayer coherence $\Delta \equiv h^{\rm mf}_{\rm eh} = |\Delta| e^{i\phi}$ will spontaneously arise, break the electron-hole U(1) symmetry, and leave only the total charge conservation. In addition, the interlayer coherence $\Delta$ will also gap out the Fermi surfaces and drive the system into an excitonic insulator phase [18]. Due to the spontaneous symmetry breaking, the long-wave phase fluctuation of the excitonic order parameter in real space $\delta\phi(\boldsymbol{r})$ is the Goldstone mode and is related to the exciton superfluidity. In real materials, a tiny single-particle tunneling $t$ is unavoidable, which breaks the electron-hole U(1) symmetry initially. This will pin the phase of the interlayer coherence to $\phi = \arg t$, gap out the zero-energy Goldstone mode, and destroy the exciton superfluidity [19–21]. Without a dielectric spacer, the single-particle tunneling strength in TMDs bilayer is on the order of 10 meV [21,22]. By inserting a few-layer hexagonal boron nitride (hBN) spacer between the two TMD single layers, the inter-layer hopping strength will be exponentially suppressed. The charge transfer time through a 1 nm thick hBN barrier was found to be about $\tau = 500$ ps, which is over 3 orders of magnitude slower than that between TMD layers without a spacer [23]. And the tunneling strength is just estimated as $t \approx \hbar/\tau \approx 0.01$ meV, which is also 3 orders lower. In addition to the phase pinning effect, the interlayer tunneling will also induce a tunneling current when the circuit is closed, which drives the system into a nonequilibrium state. However, as long as $t$ is small enough, the tunneling current is insignificant, and the nonequilibrium transport physics can be ignored.

When magnetic field is applied along the $z$ direction, the parabolic dispersions of electron and holes are quantized into Landau levels (LLs). At the CNP, the overall chemical potential must lie between the electron and hole LLs with the same index as illustrated in Fig. 1(c). The low-energy excitations are free particle-hole pairs between the highest occupied electron LL and the highest empty hole LL. When interaction is considered, such free pairs will bind to form an exciton of LLs with binding energy $E_B$. By tuning the magnetic field $B$ or exciton chemical potential $\mu_{\rm ex}$ to make the exciton binding energy $E_B$ larger than the gap between the highest occupied electron and empty hole LLs, excitons

*ylshao@iphy.ac.cn
†daix@ust.hk

 

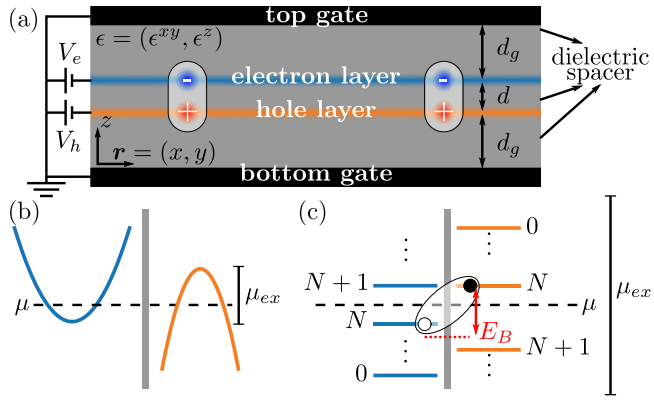


FIG. 1. (a) Setup of the double-gated electron-hole bilayer system. $d$ is the geometry distance between the electron-hole layers. The distances between the top and bottom gates and the electron and hole layers are set to be equal to $d_g$. The voltages applied to the two layers, $V_e$ and $V_h$, are used to tune the overall chemical potential and the exciton chemical potential. (b) The exciton chemical potential $\mu_{\rm ex} = eV_b - E_g$ is determined by the interlayer bias voltage $V_b = V_h - V_e$, while the overall chemical potential $\mu$ is tuned by $(V_e + V_h)/2$ to make the system charge neutral. (c) When a magnetic field is applied in the $z$ direction, the noninteracting electron and hole bands are quantized to LLs. At the CNP, the overall chemical potential must lie between the electron and hole LLs with the same index, for example, the $N$th level. If the electron-hole interaction is considered, particle-hole excitations will bind to form an exciton with binding energy $E_B$. If the gap between the $N$th electron and hole LLs is smaller than $E_B$, such an exciton of LLs will spontaneously form and condense.

of LLs will spontaneously form and condense. Since the gap between the highest electron and hole LLs will oscillate with $1/B$ and $\mu_{\rm ex}$, the physical properties of the exciton condensation state will also oscillate. As an insulator, the conventional quantum oscillation of resistance might be hard to detect. In our paper, we will focus on the interlayer capacitance

$$C_I = e^2 \left( \frac{\partial n_{\rm ex}}{\partial \mu_{\rm ex}} \right)_T \tag{1}$$

to show the quantum oscillation phenomenon in such an excitonic insulating electron-hole bilayer system.

There are several advantages of the interlayer capacitance measurement. First, it is unique to the bilayer system and can be measured accurately in real experiments [15]; i.e., by applying an ac voltage $\mathrm{d}V_b$ in one layer and measuring the differential charge density $\mathrm{d}n$ in the other layer, the interlayer capacitance is directly determined by definition as $C_I = e\mathrm{d}n/\mathrm{d}V_b$. In addition, as we will show, the oscillation behaviors of the interlayer capacitance could help us to distinguish an excitonic gap from a single-particle one. When the magnetic field is so large that the cyclotron energy $\hbar(\omega_e + \omega_h)$ is much larger than the exciton binding energy, one can always tune the exciton chemical potential $\mu_{\rm ex}$ to make $E_B$ smaller than the LL direct gap, and the exciton will not spontaneously generate and condense anymore. For such a situation, the bilayer system in the magnetic field is just two independent quantum Hall (QH) liquids and is charge incompressible at zero temperature [24], which results in a zero interlayer capacitance $C_I(T = 0) = 0$. In other words, the interlayer coherence $\Delta$ of an excitonic insulator can be destroyed by a strong magnetic field, and the interlayer capacitance might oscillate to zero. However, for a consistent hybridization from single-particle tunneling, the interlayer capacitance will never be zero.

## II. MODEL AND MEAN-FIELD THEORY

In general, the TMDs have complicated spin-valley structures. When both spin and valley degrees of freedom are considered, the lowest exciton level is approximated fourfold degenerate. However, at an appropriate interlayer distance and exciton chemical potential, which is usually satisfied in experiments, this degeneracy is lifted due to the spontaneous breaking of the time-reversal symmetry, and the exciton condensation problem will be relevant to only the two bands that form the lifted exciton energy level with the lowest energy [8]. Without magnetic field, the many-body Hamiltonian for the bilayer system as illustrated in Fig. 1(a) is modeled as [25]

$$H_0 = \sum_{ss'=eh,\boldsymbol{k}} \left( h^0_{ss'\boldsymbol{k}} - \mu\delta_{ss'} \right) c^\dagger_{s\boldsymbol{k}} c_{s'\boldsymbol{k}}, \tag{2a}$$

$$H_I = \frac{1}{2\mathcal{V}} \sum_{ss'=eh} \sum_{\boldsymbol{k}_1\boldsymbol{k}_2\boldsymbol{q}} V_{ss'}(\boldsymbol{q}) c^\dagger_{s\boldsymbol{k}_1} c^\dagger_{s'\boldsymbol{k}_2} c_{s'\boldsymbol{k}_2+\boldsymbol{q}} c_{s\boldsymbol{k}_1-\boldsymbol{q}}, \tag{2b}$$

where $c^\dagger_{e\boldsymbol{k}}$ and $c^\dagger_{h\boldsymbol{k}}$ are electron creation operators in the electron and hole layers, $\mathcal{V} \equiv L_x L_y$ is the area of the two-dimensional (2D) system, and $L_i$ is the system length in the $i$ direction. The spin-valley structures of the electron and hole bands are related to the true ground state after the breaking of time-reversal symmetry. Since they do not affect the exciton condensation and quantum oscillation physics, the spin and valley indices will be abbreviated in this paper. Under $k \cdot p$ approximation, the single-particle Hamiltonian is

$$h^0_{\boldsymbol{k}} = \begin{bmatrix} \hbar^2 k^2/2m_e - \mu_{\rm ex} & t \\ t^* & -\hbar^2 k^2/2m_h \end{bmatrix}, \tag{3}$$

where $m_{e/h}$ are the effective masses and $t$ is the interlayer tunneling strength. The intra- and interlayer interactions are taken as the gate-screened Coulomb interactions [26] $V(q) \equiv V_{s=s'}(q) \approx 2\pi e^2/\epsilon q(1 - e^{-2\kappa q d_g})$ and $U(q) \equiv V_{s\neq s'}(q) \approx V(q)e^{-\kappa q d}$, where $\epsilon = \sqrt{\epsilon^{xy}\epsilon^z}$ is the effective dielectric constant and $\kappa \equiv \sqrt{\epsilon^{xy}/\epsilon^z}$ is the anisotropy parameter (a detailed derivation is given in Appendix A).

By assuming a nonzero EI order parameter $\rho_{eh\boldsymbol{k}}$, where $\rho_{ss'\boldsymbol{k}} \equiv \langle c^\dagger_{s'\boldsymbol{k}} c_{s\boldsymbol{k}} \rangle - \delta_{ss'}\delta_{sh}$ is the density matrix relative to the uncharged state ($\rho_0 = \delta_{ss'}\delta_{sh}$ is subtracted to avoid double counting [8,27]), the interacting part of the many-body Hamiltonian (2) is decoupled into a noninteracting mean-field Hamiltonian

$$H_{\rm MF} = \sum_{ss'\boldsymbol{k}} \left( h^0_{ss'\boldsymbol{k}} + h^H_{ss'} + h^F_{ss'\boldsymbol{k}} - \mu\delta_{ss'} \right) c^\dagger_{s\boldsymbol{k}} c_{s'\boldsymbol{k}}. \tag{4}$$

The Hartree and Fock terms are constructed by a density matrix as

$$h^H = \frac{e^2 n_{\rm ex}}{2C_{\rm geo}} \sigma_z, \tag{5a}$$

$$h^F_{ss'\boldsymbol{k}} = -\frac{1}{\mathcal{V}} \sum_{\boldsymbol{k}} V_{ss'}(\boldsymbol{k} - \boldsymbol{k}') \rho_{ss'\boldsymbol{k}'}, \tag{5b}$$

where $\sigma_z$ is the Pauli matrix, $n_{\rm ex} = \mathcal{V}^{-1}\sum_{\boldsymbol{k}} \rho_{ee\boldsymbol{k}}$ is exciton density, and $C_{\rm geo} = \epsilon^z/4\pi d$ is the geometry capacitance of the charged electron-hole double layer. The mean-field Hamiltonian $h^{\rm mf}_{\boldsymbol{k}} = h^0_{\boldsymbol{k}} + h^H + h^F_{\boldsymbol{k}}$ is a $2\times 2$ matrix and has two eigenvalues:

$$h^{\rm mf}_{\boldsymbol{k}}|c/v,\boldsymbol{k}\rangle = \xi_{c/v,\boldsymbol{k}}|c/v,\boldsymbol{k}\rangle, \tag{6}$$

where $\xi_{c,\boldsymbol{k}} > \xi_{v,\boldsymbol{k}}$ are the mean-field energy bands and $|c/v,\boldsymbol{k}\rangle$ are the corresponding eigenstates. Then a new density matrix can be reconstructed as

$$\rho_{\boldsymbol{k}} = \sum_{i=c,v} f_{i,\boldsymbol{k}}(\mu)|i,\boldsymbol{k}\rangle\langle i,\boldsymbol{k}| - \delta_{ss'}\delta_{sh}, \tag{7}$$

where $f_{i,\boldsymbol{k}}(\mu) = 1/[1+e^{(\xi_{i,k}-\mu)/k_BT}]$ are the occupation numbers. By requiring charge neutrality, the overall chemical potential is determined by solving

$$\sum_{\boldsymbol{k}}[f_{c,\boldsymbol{k}}(\mu) + f_{v,\boldsymbol{k}}(\mu) - 1] = 0. \tag{8}$$

Equations (5)–(8) form the full self-consistent procedure. At zero temperature $T = 0$, Eq. (8) is simply solved as $f_{c,\boldsymbol{k}} = 0$ and $f_{v,\boldsymbol{k}} = 1$. Such a mean-field procedure is equivalent to minimizing the free energy $F[|c/v,\boldsymbol{k}\rangle, f_{c/v,\boldsymbol{k}}; T, \mu_{\rm ex}] = U - TS$ with respect to the wave functions $|c/v,\boldsymbol{k}\rangle$ and occupation numbers $f_{c/v,\boldsymbol{k}}$ under constraints $\langle i,\boldsymbol{k}|j,\boldsymbol{k}\rangle = \delta_{ij}$ and $\sum_{\boldsymbol{k}}{\rm Tr}\rho_{\boldsymbol{k}} = 0$, where $U$ and $S$ are internal energy and entropy, defined as

$$U = \frac{1}{2}\sum_{\boldsymbol{k}}{\rm Tr}\big[\big(h^0_{\boldsymbol{k}} + h^{\rm mf}_{\boldsymbol{k}}\big)\rho_{\boldsymbol{k}}\big], \tag{9}$$

$$S = -k_B\sum_{i,\boldsymbol{k}}[f_{i,\boldsymbol{k}}\ln f_{i,\boldsymbol{k}} + (1-f_{i,\boldsymbol{k}})\ln(1-f_{i,\boldsymbol{k}})]. \tag{10}$$

Proof of the equivalence is given in Appendix B.

When a magnetic field is applied along the $z$ direction, it is more convenient to adopt the LL basis. In the Landau gauge $\boldsymbol{A} = (-yB, 0)$, the parabolic bands are quantized into LLs $|\phi_{nk_x}\rangle$, as shown in Fig. 1(c), where $n$ is the LL index and $k_x$ is the momentum in the $x$ direction. By defining the creation operator for LL electrons $l^\dagger_{snk_x} \equiv \sum_{\boldsymbol{k}'}\langle\boldsymbol{k}'|\phi_{nk_x}\rangle c^\dagger_{s\boldsymbol{k}'}$, which, in fact, is a basis transformation, the many-body Hamiltonian with magnetic field is written under the LL basis as

$$H_0 = \sum_{ss'nk_x}\big(h^0_{n,ss'} - \mu\delta_{ss'}\big)l^\dagger_{snk_x}l_{s'nk_x}, \tag{11a}$$

$$H_I = \frac{1}{2\mathcal{V}}\sum_{ss'n_ik_i}\sum_{\boldsymbol{q}} V_{ss'}(\boldsymbol{q})e^{iq_y(k_1-k_2)\ell^2}\Lambda^*_{n_4n_1}(\boldsymbol{q})\Lambda_{n_2n_3}(\boldsymbol{q}) \times l^\dagger_{sn_1k_1+q_x/2}l^\dagger_{s'n_2k_2-q_x/2}l_{s'n_3k_2+q_x/2}l_{sn_4k_1-q_x/2}, \tag{11b}$$

where $\ell = \sqrt{\hbar/eB}$ is the magnetic length and $\Lambda_{mn}(\boldsymbol{q})$ is the form factor of the LLs, defined as [28]

$$\Lambda_{mn}(\boldsymbol{q}) \equiv \langle\phi_{mk-q_x/2}|e^{-i\boldsymbol{q}\cdot\boldsymbol{r}}|\phi_{nk+q_x/2}\rangle e^{ikq_y\ell^2}. \tag{12}$$

The single-particle Hamiltonian now becomes

$$h^0_n = \begin{bmatrix}\hbar\omega_e(n+1/2) - \mu_{\rm ex} & t\\ t^* & -\hbar\omega_h(n+1/2)\end{bmatrix}, \tag{13}$$

where $\omega_s \equiv eB/m_s$ is the cyclotron frequency. The details of deriving Eq. (11) are given in Appendix C. In addition to the Landau quantization of the electron and hole bands, the Zeeman effect will also help fix the spin structures of the electron and hole bands [8]; i.e., the electron band has an up spin, while the hole band prefers a down spin. Then the valley indices of the two bands will be automatically fixed due to the spin-valley locking physics in TMDs [29]. In addition, the Zeeman energies can be absorbed in the definition of $\mu_{\rm ex}$ and will not be written out explicitly.

The density matrix is now defined as $\rho_{sn_1,s'n_2}(k_x) \equiv \langle l^\dagger_{s'n_2k_x}l_{sn_1k_x}\rangle - \delta_{ss'}\delta_{sh}$. However, due to symmetry constraints, not all the elements survive. Although the vector potential in the Landau gauge $\boldsymbol{A} = (-yB, 0)$ breaks translation symmetry in the $y$ direction, the physics is expected to be independent of the choice of the gauge. After a small translation in the $y$ direction, i.e., $\boldsymbol{A} \to (-(y-\eta)B, 0)$, the magnetic field is invariant, while the LL electron transforms as $l^\dagger_{snk_x} \to l^\dagger_{snk_x+eB\eta/\hbar}$. It is easy to see that the many-body Hamiltonian (11) is invariant under such a magnetic translation, while the density matrix transforms from $\rho_{sn_1,s'n_2}(k_x)$ to $\rho_{sn_1,s'n_2}(k_x + eB\eta/\hbar)$. By requiring magnetic translation symmetry in the $y$ direction, the density matrix should be $k_x$ independent, i.e., $\rho_{sn_1,s'n_2}(k_x) = \rho_{sn_1,s'n_2}$. As discussed in Appendix D, when magnetic translation symmetry is preserved, the EI order parameters $\rho_{en_1,hn_2}$ can be decomposed into independent channels labeled by their angular momenta $M \equiv n_1 - n_2$. In the charge-neutral case, the overall chemical potential $\mu$ must lie between electron and hole LLs with the same index, for example, the $N$th level, as illustrated in Fig. 1(c). At this time, the $s$-wave pairing case with zero angular momentum $M = 0$ usually has the lowest energy. For electron and hole bands with trivial band topology, high angular momentum exciton condensation in the quantum Hall regime is energetically preferable only when the electron and hole layers are charge imbalanced, as investigated by Zou *et al.* [30]. In summary, by requiring magnetic translation symmetry and $s$-wave pairing, the only surviving density matrix elements are $\rho_{sn,s'n}$, and they will be abbreviated as $\rho_{n,ss'}$ in the following.

Once the mean-field channels are determined, the Hartree-Fock procedure is straightforward, and the mean-field Hamiltonian in the LL basis is written as

$$H_{\rm MF} = \sum_{ss'nk_x}\big(h^0_{n,ss'} + h^H_{ss'} + h^F_{n,ss'} - \mu\delta_{ss'}\big)l^\dagger_{snk_x}l_{s'nk_x}. \tag{14}$$

Since the Hartree term is just a renormalization of the exciton chemical potential due to the geometry electrostatic energy, it is independent of basis transformation and is still given by Eq. (5a). The only difference is that the exciton density is calculated as $n_{\rm ex} = (2\pi\ell^2)^{-1}\sum_n \rho_{n,ee}$. The Fock term becomes

$$h^F_{n,ss'} = -\sum_{n'} V_{ss',nn'}\rho_{n',ss'}, \tag{15}$$

where $V_{ss',nn'} = \mathcal{V}^{-1}\sum_{\boldsymbol{q}} V_{ss'}(q)|\Lambda_{n'n}(\boldsymbol{q})|^2$ is the interaction matrix elements projected to the LL basis. By replacing the $\boldsymbol{k}$ index in (6)–(8) with the LL index $n$, we get the full self-consistent equations under the LL basis.

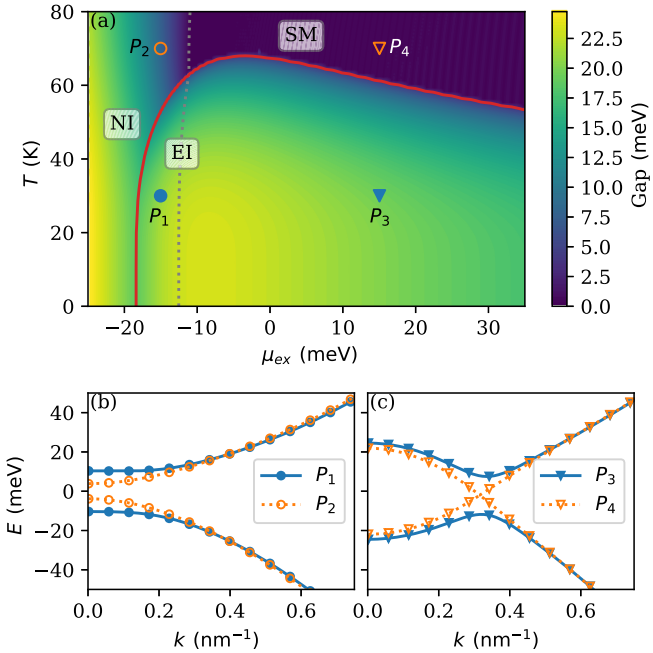


FIG. 2. (a) Zero magnetic field phase diagram as a function of the exciton chemical potential $\mu_{\rm ex}$ and temperature $T$; the single-particle tunneling strength $t$ is assumed to be zero. Below the red solid line, the EI order parameter is not zero, i.e., $\rho_{\rm eh} \neq 0$, which means the system is in the EI phase, while above the red solid line $\rho_{\rm eh} = 0$ and the system is in the normal phase. The gray dashed line further separates the normal phase into a NI phase and a SM phase. In the NI phase, there is no inversion between the renormalized electron and hole bands, while in the SM phase electron and hole bands are inverted. The color represents the mean-field band gap. (b) and (c) Typical mean-field band structures in different regions of the parameter space; points $P_{1-4}$ in (a) are used as examples.

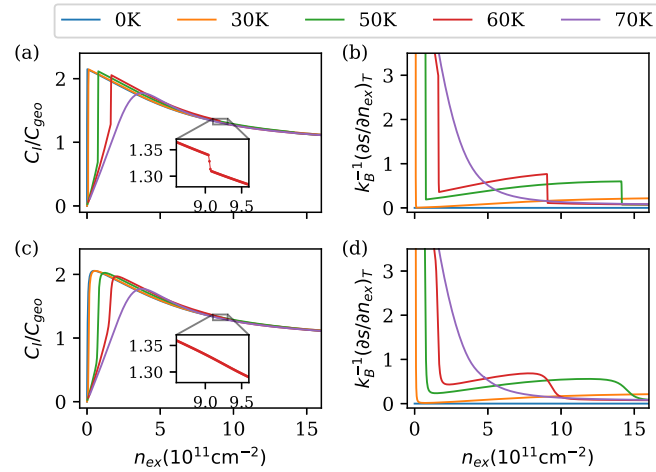


FIG. 3. (a) Interlayer capacitance as a function of exciton density and temperature. The inset shows a magnified view of the line at 60 K near the phase boundary between the EI and SM phases, which has a discontinuous feature. (b) Entropy change per exciton $(\partial s/\partial n_{\rm ex})_T$ as a function of exciton density and temperature, which shows the discontinuities between the EI and SM phases more clearly. (c) and (d) The same quantities as in (a) and (b) except that a finite single-particle tunneling strength $t \approx 0.01$ meV instead $t = 0$ meV is used.

## III. RESULTS

In our calculation, the parameters are set to be consistent with the $MoSe_2$/hBN/$WSe_2$ heterostructure experimentally studied by Ma *et al.* [15]. The effective masses of the conduction band minimum of $MoSe_2$ and valence band maximum of $WSe_2$ in the $K$-valley centers are about $m_e \approx 0.58m_0$ and $m_h \approx 0.36m_0$ [31] ($m_0$ is the bare electron mass). The interlayer and gate-layer distances are taken as $d \approx 2.5$ nm (five- to six-layer hBN spacer) and $d_g \approx 10$ nm. The dielectric constant of hBN is about $\epsilon^{xy} \approx 6.71$ and $\epsilon^{z} \approx 3.57$ [32]. Thus, the anisotropy parameter and the effective dielectric constant are about $\kappa \approx 1.37$ and $\epsilon \approx 4.89$. To fit the interlayer exciton binding energy in the experiment [15] (about 20 meV), a larger effective dielectric constant, $\epsilon = 9$, is used in the calculation.

### A. Interlayer capacitance at zero magnetic field

Let us first ignore the single-particle tunneling $t$. At zero magnetic field, the mean-field phase diagram as a function of the exciton chemical potential $\mu_{\rm ex}$ and temperature $T$ is calculated and plotted in Fig. 2(a). The red solid line is the boundary of the region $\rho_{\rm eh}(T, \mu_{\rm ex}) \neq 0$. The area below the red line is the EI phase with a nonzero order parameter $\rho_{\rm eh} \neq 0$. However, above the red line, there is no EI order, and the system is in the normal phase. The gray dashed line is determined by requiring the renormalized offset between the electron and hole bands to be equal to the original gap, after which the inversion between the renormalized conduction and valence bands from different layers occurs. To the left of the gray dashed line, there is no band inversion, and the normal phase is just a normal insulator (NI); to the right of this line, the normal phase is a semimetal (SM). In the EI phase, the gray dashed line does not mark a phase transition but, rather, indicates a Bose-Einstein condensate to BCS crossover to some extent. By diagonalizing the mean-field Hamiltonian $h_{\boldsymbol{k}}^{\rm mf}$, mean-field band structures are obtained, and the gap is represented by the color plot in Fig. 2(a). In addition, typical mean-field band structures in different regions of the parameter space are also plotted in Figs. 2(b) and 2(c) [points $P_{1-4}$ in Fig. 2(a) are used as examples].

At the CNP, the interlayer capacitance $C_I$ (in units of the geometry capacitance $C_{\rm geo} = \epsilon^z/4\pi d$) is calculated and plotted in Fig. 3(a) as a function of the exciton density (the abscissa) and temperature (different colored lines). The inset in Fig. 3(a) shows a magnified view of the line near the phase boundary between the EI phase and the SM phase at 60 K. Due to the exchange part of the interaction, which accounts for exciton condensation, the interlayer capacitance is greatly enhanced from its classic geometry value, which is consistent with previous studies [8,25]. In addition, discontinuities of $C_I$ are shown at the transition points between EI and normal phases. To see the discontinuities between the EI and SM phases more clearly, the entropy change per exciton $(\partial s/\partial n_{\rm ex})_T$ is calculated and plotted in Fig. 3(b), where $s \equiv S/\mathcal{V}$ is the entropy density and $S$ is calculated using Eq. (10). However, these discontinuities may be absent in real experiments. On the one hand, the transition between an EI and NI in the low-density region at finite temperature is a

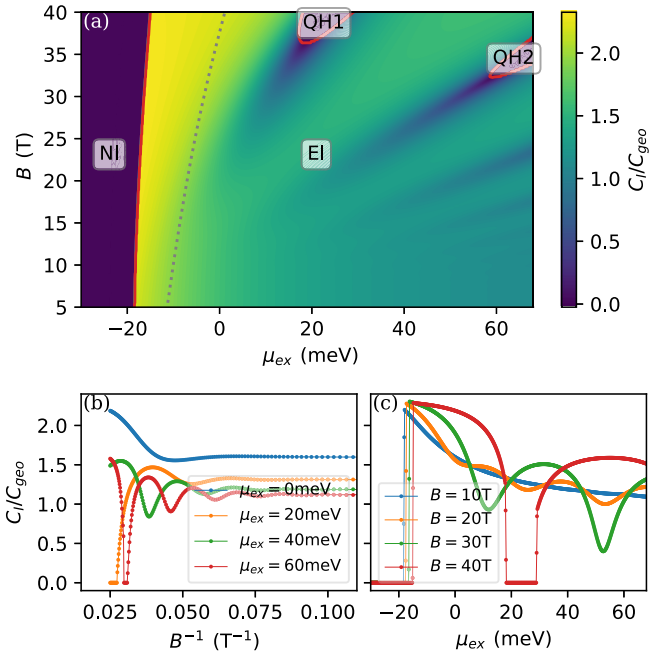


FIG. 4. (a) Phase diagram as a function of the exciton chemical potential $\mu_{\rm ex}$ and magnetic field strength $B$ at 0 K. The single-particle tunneling strength is assumed to be zero. The red solid line separates the region into an EI phase with a nonzero EI order parameter $\rho_{\rm eh} \neq 0$ and normal phases with $\rho_{\rm eh} = 0$. The gray dashed line is the critical line for band inversion. In the NI phase, all hole LLs are occupied, and all electron LLs are empty. In the QH$N$ phases, the first $N$ electron LLs are occupied, while the first $N$ hole LLs are empty. The pseudo color map represents the interlayer capacitance $C_I/C_{\rm geo}$. (b) and (c) Oscillations of interlayer capacitance $C_I$ versus $B^{-1}$ and $\mu_{\rm ex}$, respectively.

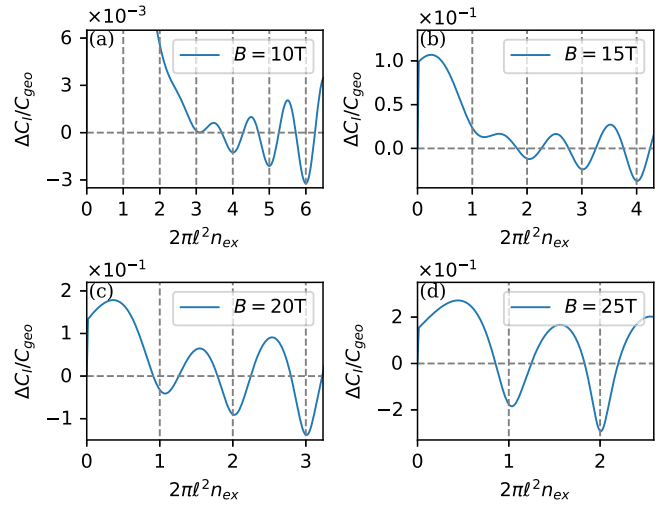


FIG. 5. Oscillations of $\Delta C_I(n_{\rm ex}, B)$ versus $n_{\rm ex}$ for different magnetic field strengths.

Berezinskii-Kosterlitz-Thouless (BKT) transition [7,33] that is beyond the mean-field description, and its main effect is to smooth out the dramatic changes in the mean-field theory. On the other hand, these discontinuities are easily smoothed by a very small single-particle tunneling effect. In Figs. 3(c) and 3(d), the same quantities as in Figs. 3(a) and 3(b) are plotted, except that a finite single-particle tunneling strength $t = 0.01$ meV is used. Although the tunneling strength $t$ is much smaller than the mean-field gap [about 20 meV, as indicated in Fig. 2(a)], the discontinuities at the EI phase boundary no longer exist, as shown in Figs. 3(c) and 3(d).

### B. Quantum oscillation of the interlayer capacitance

Since the interlayer tunneling gaps out the Goldstone mode, the BKT phenomenon is suppressed for temperatures much below the energy scale of the tunneling strength $t$, especially at zero temperature. In this situation, the mean-field theory is still qualitatively right. Thus, in this part, we will focus on zero temperature. Ignoring the single-particle tunneling effect, the mean-field phase diagram as a function of the exciton chemical potential $\mu_{\rm ex}$ and magnetic field strength $B$ is plotted in Fig. 4(a). Like in Fig. 2(a), the red solid line is the boundary of the region $\rho_{\rm eh} \neq 0$, and the gray dashed line is the critical line for band inversion. Only in the EI phase does $\rho_{\rm eh} \neq 0$, and there is interlayer coherence. In the NI phase, there is no band inversion between the electron and hole bands in which all the hole LLs are occupied and the electron LLs are empty. In the QH phase, according to the index $N$ of the highest inverted electron and hole LLs, the regions in the parameter space are labeled by QH$N$, as shown in Fig. 4(a). The color in Fig. 4(a) represents the interlayer capacitance $C_I/C_{\rm geo}$, which is plotted in more detail in Figs. 4(b) and 4(c). Oscillations versus $B^{-1}$ and $\mu_{\rm ex}$ are easily identified. Similar to the quantum oscillation in metal, the oscillation frequency versus $B^{-1}$ increases with exciton chemical potential, as shown in Fig. 4(b). It is also worth noting that interlayer capacitance sharply oscillates to zero in the QH phases, which reflects the fact that a QH state is charge incompressible at zero temperature. To see the oscillations versus $\mu_{\rm ex}$ more clearly, let us transform the abscissa from $\mu_{\rm ex}$ to $n_{\rm ex}$ and define $\Delta C_I(n_{\rm ex}, B)$ as

$$\Delta C_I(n_{\rm ex}, B) \equiv C_I(n_{\rm ex}, B) - C_I(n_{\rm ex}, B = 0). \tag{16}$$

Then the oscillations of $\Delta C_I$ versus $n_{\rm ex}$ are shown in Figs. 5(a)–5(d) for different magnetic field strengths. A period of about $(2\pi\ell^2)^{-1} = eB/h$ is observed, which is exactly the LL degeneracy for a spinless fermion.

When the finite, but small, tunneling strength $t = 0.01$ meV is considered, the phase transitions between the NI, EI, and QH phases become continuous crossovers, and the discontinuities in Figs. 4(b) and 4(c) are also smoothed, just like in the case without magnetic field. In addition, the oscillation amplitudes also get slightly smaller. The corresponding numerical results are given in Appendix E for reference.

## IV. SUMMARY AND DISCUSSION

For an electron-hole bilayer without any interlayer coupling, the system is just a semimetal, and quantum oscillations are not surprising due to the Landau quantization of the electron and hole Fermi surfaces [34]. An interband hybridization $h_{\rm eh}$ will gap out the Fermi surfaces and lead the system into an insulating phase at the CNP. However, as long as the hybridization strength is comparable to the cyclotron

frequency $\hbar(\omega_e+\omega_h)$, quantum oscillations of physical quantities are still expected. Such oscillations have already been predicted [35–39] and detected [40–43] in narrow-gap insulators where the hybridization has a single-particle origination. However, in this paper, we showed that quantum oscillations will also appear in EI systems where the interband hybridization arises purely from exciton condensation.

A more interesting observation is the QH phases in the phase diagram in Fig. 4(a), where there is no EI order parameter. These phases are also noted in a similar study by Zou *et al.* [30]. From the physical picture of an exciton formed by electron and hole LLs illustrated in Fig. 1(c), the critical magnetic field strength can be estimated by requiring the cyclotron frequency to be comparable to the exciton binding energy, i.e., $\hbar(\omega_e+\omega_h)/2=E_B$, which implies

$$B_c=\frac{2m_em_h}{m_e+m_h}\frac{E_B}{e\hbar}. \tag{17}$$

Substituting the parameters $m_e=0.58m_0$ and $m_h=0.36m_0$ and the value of the zero-density binding energy $E_B\approx 20$ meV into Eq. (17), the critical field strength is estimated as $B_c\approx 77$ T. We argue that this value is an overestimation since the binding energy usually drops with the increase of the exciton density $n_{\rm ex}$ (or, equivalently, the exciton chemical potential $\mu_{\rm ex}$) [25]. This point can also be seen from the fact that the critical field strength of the QH2 phase is lower than that of the QH1 phase. Such QH phases are also unique to the 2D system. In three-dimensional cases, the electron and hole LLs are usually dispersive in the third dimension, like in Fig. 1(b). In the BCS regime where electron and hole bands are inverted, the subbands of LLs are also inverted, and the Fermi surface instability will always drive the system into the EI phase [44–47].

The emergence of the QH phases also reflects the instability of an excitonic gap, which can be destroyed not only by temperature [18] and electrical field [48] but also by magnetic field in 2D systems. This instability is a key difference between an exciton gap and a single-particle gap and can easily be identified in interlayer capacitance measurements. As shown in Figs. 4(b) and 4(c), the interlayer capacitance at zero temperature oscillates to zero when the EI order and interband hybridization are destroyed by the magnetic field in the QH phases. However, the capacitance will never be zero if the gap has a single-particle origination as derived in Appendix F. Furthermore, a zero interlayer capacitance in a strong magnetic field could be used to exclude the single-particle contribution to the excitonic gap, which is an essential requirement for exciton superfluidity.

## ACKNOWLEDGMENTS

We thank Prof. K. F. Mak for helpful discussions. This work was fully supported by a fellowship award from the Research Grants Council of the Hong Kong Special Administrative Region, China (Project No. C7037-22GF).

## APPENDIX A: GATE SCREENING INTERACTION

When the gate layer distance $d_g$ is comparable to the interlayer distance $d$, the screening effects from the gates are not negligible. To derive the gate screening interaction, let us solve the Poisson equation of a point charge. For convenience, let us assume the point charge is in the electron layer; using the Dirichlet boundary condition, the Poisson equation reads

$$\epsilon^{xy}\nabla_{\boldsymbol{r}}^2\varphi(\boldsymbol{r},z)+\epsilon^z\partial_z^2\varphi(\boldsymbol{r},z)=-4\pi e\delta(\boldsymbol{r}-\boldsymbol{r}_0)\delta(z-d-d_g),$$
$$\boldsymbol{\nabla}_{\boldsymbol{r}}\varphi(\boldsymbol{r},z)|_{z=0,d+2d_g}=\boldsymbol{0}.$$

If we define the 2D Fourier transformation of $\varphi(\boldsymbol{r},z)$ as $\varphi_{\boldsymbol{q}}(z)=\int d\boldsymbol{r}\,\varphi(\boldsymbol{r},z)e^{-i\boldsymbol{q}\cdot\boldsymbol{r}}$, the Poisson equation becomes

$$\epsilon^z\partial_z^2\varphi_{\boldsymbol{q}}(z)-q^2\epsilon^{xy}\varphi_{\boldsymbol{q}}(z)=-4\pi e\delta(z-d-d_g), \tag{A2a}$$
$$\varphi_{\boldsymbol{q}}(z=0,d+2d_g)=0. \tag{A2b}$$

If we define the effective dielectric constant and anisotropy parameter as $\epsilon=\sqrt{\epsilon^{xy}\epsilon^z}$ and $\kappa=\sqrt{\epsilon^{xy}/\epsilon^z}$, the Poisson equation (A2) is solved as

$$\varphi_{\boldsymbol{q}}(z)=\frac{2\pi}{\epsilon q}[c_1e^{\kappa qz}+c_2e^{-\kappa qz}+e^{-\kappa q|z-(d+d_g)|}],$$
$$c_1=-\frac{e^{-\kappa q(2d_g+d)}\sinh\kappa q(d_g+d)}{\sinh\kappa q(2d_g+d)},$$
$$c_2=-\frac{\sinh\kappa qd_g}{\sinh\kappa q(2d_g+d)}.$$

Thus, the intra- and interlayer interactions are

$$V_{\rm intra}(\boldsymbol{q})=e\varphi_{\boldsymbol{q}}(d+d_g)=\frac{4\pi e^2}{\epsilon q}\frac{\sinh\kappa qd_g\sinh\kappa q(d+d_g)}{\sinh\kappa q(2d_g+d)}, \tag{A3a}$$

$$V_{\rm inter}(\boldsymbol{q})=e\varphi_{\boldsymbol{q}}(d_g)=\frac{4\pi e^2}{\epsilon q}\frac{\sinh^2\kappa qd_g}{\sinh\kappa q(2d_g+d)}. \tag{A3b}$$

Expanded in exponentials, the interactions are approximated by

$$V_{\rm intra}(\boldsymbol{q})\approx\frac{2\pi e^2}{\epsilon q}\left(1-e^{-2\kappa qd_g}\right), \tag{A4a}$$

$$V_{\rm inter}(\boldsymbol{q})\approx\frac{2\pi e^2}{\epsilon q}\left(1-e^{-2\kappa qd_g}\right)e^{-\kappa qd}. \tag{A4b}$$

From the expression in Eq. (A4) we can see that the screening mainly happens in the long-range part ($q\to 0$) of the interaction.

## APPENDIX B: MINIMIZATION OF THE FREE ENERGY

In this appendix, we will derive the self-consistent equations by minimizing the free energy. For simplicity, only the derivations for the case without magnetic field are presented.

At fixed temperature $T$ and exciton chemical potential $\mu_{\rm ex}$, the free energy $F=U-TS$ is a functional of the wave functions $|i=c/v,\boldsymbol{k}\rangle$ and occupation numbers $f_{i,\boldsymbol{k}}$ of the mean-field bands, where the internal energy $U$ and entropy $S$ are respectively written as

$$U=\frac{1}{2}\sum_{\boldsymbol{k}}\mathrm{Tr}\left[\left(h_{\boldsymbol{k}}^0+h_{\boldsymbol{k}}^{\rm mf}\right)\rho_{\boldsymbol{k}}\right], \tag{B1}$$

$$S=-k_B\sum_{i,\boldsymbol{k}}[f_{i,\boldsymbol{k}}\ln f_{i,\boldsymbol{k}}+(1-f_{i,\boldsymbol{k}})\ln(1-f_{i,\boldsymbol{k}})], \tag{B2}$$

and $\rho_{\boldsymbol{k}}$ is the density matrix relative to the uncharged state $\rho_0 = \delta_{ss'}\delta_{sh}$, which is defined by

$$\rho_{\boldsymbol{k}}[|i,\boldsymbol{k}\rangle, f_{i,\boldsymbol{k}}] = \sum_{i=c,v} f_{i,\boldsymbol{k}}|i,\boldsymbol{k}\rangle\langle i,\boldsymbol{k}| - \delta_{ss'}\delta_{sh}. \tag{B3}$$

There are two kinds of constraints. The first one is the orthonormal relation of the wave functions,

$$\langle i,\boldsymbol{k}|j,\boldsymbol{k}\rangle = \delta_{ij}, \tag{B4}$$

and the second one is the charge neutrality requirement,

$$\sum_{\boldsymbol{k}} \mathrm{Tr}(\rho_{\boldsymbol{k}}) = \sum_{\boldsymbol{k}} (f_{c,\boldsymbol{k}} + f_{v,\boldsymbol{k}} - 1) = 0. \tag{B5}$$

It is more convenient to introduce the Lagrange multipliers $\xi_{i,\boldsymbol{k}}$ (the mean-field band energies) and $\mu$ (overall chemical potential) and transform the constrained minimization of the free energy to an unconstrained minimization of the grand potential

$$G \equiv F - \sum_{i,\boldsymbol{k}} \xi_{i,\boldsymbol{k}} f_{i,\boldsymbol{k}}(\langle i,\boldsymbol{k}|i,\boldsymbol{k}\rangle - 1) - \mu \sum_{\boldsymbol{k}} (f_{c,\boldsymbol{k}} + f_{v,\boldsymbol{k}} - 1). \tag{B6}$$

Under this definition, derivatives of $G$ with respect to $\xi_{i,\boldsymbol{k}}$ and $\mu$ recover the constraints (B4) and (B5). Unconstrained derivatives of $G$ with respect to $|i,\boldsymbol{k}\rangle$ are calculated as

$$\frac{\delta G}{\delta\langle i,\boldsymbol{k}|} = \frac{\delta U}{\delta\rho_{\boldsymbol{k}}}\frac{\delta\rho_{\boldsymbol{k}}}{\delta\langle i,\boldsymbol{k}|} - \xi_{i,\boldsymbol{k}} f_{i,\boldsymbol{k}}|i,\boldsymbol{k}\rangle = f_{i,\boldsymbol{k}}\big(h^{\mathrm{mf}}_{\boldsymbol{k}} - \xi_{i,\boldsymbol{k}}\big)|i,\boldsymbol{k}\rangle. \tag{B7}$$

For $f_{i,\boldsymbol{k}} \neq 0$, the minimization condition $\delta G/\delta\langle i,\boldsymbol{k}| = 0$ leads to the eigenvalue equation

$$h^{\mathrm{mf}}_{\boldsymbol{k}}|i,\boldsymbol{k}\rangle = \xi_{i,\boldsymbol{k}}|i,\boldsymbol{k}\rangle. \tag{B8}$$

In addition, unconstrained derivatives of $G$ with respect to $f_{i,\boldsymbol{k}}$ are calculated as

$$\begin{aligned}\frac{\delta G}{\delta f_{i,\boldsymbol{k}}} &= \frac{\delta U}{\delta\rho_{\boldsymbol{k}}}\frac{\delta\rho_{\boldsymbol{k}}}{\delta f_{i,\boldsymbol{k}}} - T\frac{\delta S}{\delta f_{i,\boldsymbol{k}}} - \xi_{i,\boldsymbol{k}}(\langle i,\boldsymbol{k}|i,\boldsymbol{k}\rangle - 1) - \mu \\ &= \mathrm{Tr}\big(h^{\mathrm{mf}}_{\boldsymbol{k}}|i,\boldsymbol{k}\rangle\langle i,\boldsymbol{k}|\big) + k_B T \ln\frac{f_{i,\boldsymbol{k}}}{1-f_{i,\boldsymbol{k}}} - \mu \\ &= \xi_{i,\boldsymbol{k}} - \mu + k_B T \ln\frac{f_{i,\boldsymbol{k}}}{1-f_{i,\boldsymbol{k}}},\end{aligned} \tag{B9}$$

where the orthonormal constraints (B4) and the eigenvalue equation (B8) are used to get the final expression. Then the minimization condition $\delta G/\delta f_{i,\boldsymbol{k}} = 0$ leads to the Fermi-Dirac distribution

$$f_{i,\boldsymbol{k}} = \frac{1}{1 + e^{(\xi_{i,\boldsymbol{k}}-\mu)/k_B T}}. \tag{B10}$$

## APPENDIX C: MANY-BODY HAMILTONIAN UNDER THE LANDAU LEVEL BASIS

In this Appendix, we will derive the LL representations of the many-body Hamiltonian. When magnetic field is applied, one should replace the kinetic momentum $\hbar\boldsymbol{k}$ in Eq. (3) by the canonical momentum $\boldsymbol{\Pi} = \hbar\boldsymbol{k} + e\boldsymbol{A}$ ($e = |e|$) according to Peierls substitution [49]. In the Landau gauge $\boldsymbol{A} = (-yB, 0)$, the wave functions of LLs are

$$\phi_{nk_x}(\boldsymbol{r}) = \frac{1}{\sqrt{L_x\ell}} e^{ik_x x}\psi_n(y/\ell - \ell k_x),\ k_x \in [0, L_y/\ell^2], \tag{C1}$$

where $L_i$ is the system size in the $i$ direction, $\ell = \sqrt{\hbar/eB}$ is the magnetic length, and

$$\psi_n(x) = (2^n n!\sqrt{\pi})^{-1/2} e^{-x^2/2} H_n(x) \tag{C2}$$

is the $n$th level of the one-dimensional quantum Harmonic oscillator. The LLs are complete and orthonormal; i.e., $\langle\phi_{nk_x}|\phi_{mk'_x}\rangle = \delta_{nm}\delta_{k_x k'_x}$, and $\sum_{nk_x}|\phi_{nk_x}\rangle\langle\phi_{nk_x}| = \mathbb{1}$. Furthermore, they satisfy

$$\frac{\Pi^2}{2m_s}|\phi_{nk_x}\rangle = \hbar\omega_s(n+1/2)|\phi_{nk_x}\rangle, \tag{C3}$$

where $\omega_s = eB/m_s$ is the cyclotron frequency.

It is easy to verify that

$$\begin{aligned}\big\langle e,\phi_{nk_x}\big|h^0_{\boldsymbol{\Pi}}\big|e,\phi_{mk'_x}\big\rangle &= [\hbar\omega_e(n+1/2) - \mu_{\mathrm{ex}}]\delta_{nm}\delta_{k_x k'_x}, \\ \big\langle h,\phi_{nk_x}\big|h^0_{\boldsymbol{\Pi}}\big|h,\phi_{mk'_x}\big\rangle &= -\hbar\omega_h(n+1/2)\delta_{nm}\delta_{k_x k'_x}, \\ \big\langle e,\phi_{nk_x}\big|h^0_{\boldsymbol{\Pi}}\big|h,\phi_{mk'_x}\big\rangle &= t\,\delta_{nm}\delta_{k_x k'_x}.\end{aligned}$$

Thus, the single-particle part expressed in the LL basis is written as

$$\begin{aligned}H_0 &= \sum_{ss'nk_x}\big\langle s,\phi_{nk_x}\big|h^0_{\boldsymbol{\Pi}} - \mu\big|s',\phi_{nk_x}\big\rangle l^\dagger_{snk_x} l_{snk_x} \\ &= \sum_{ss'nk_x}\big(h^0_{n,ss'} - \mu\delta_{ss'}\big) l^\dagger_{snk_x} l_{snk_x},\end{aligned} \tag{C5}$$

where $l^\dagger_{sn_x}$ is the creation operator for LL electrons and

$$h^0_n = \begin{bmatrix}\hbar\omega_e(n+1/2) - \mu_{\mathrm{ex}} & t \\ t^* & -\hbar\omega_h(n+1/2)\end{bmatrix}. \tag{C6}$$

Using the relation

$$c_{s\boldsymbol{k}} = \sum_{nk'_x}\langle\boldsymbol{k}|\phi_{nk'_x}\rangle l_{snk'_x}, \tag{C7}$$

the interaction part [Eq. (2b)] becomes

$$\begin{aligned}H_I &= \frac{1}{2\mathcal{V}}\sum_{ss'}\sum_{\boldsymbol{k}'_1\boldsymbol{k}'_2\boldsymbol{q}}\sum_{n_i k_i} V_{ss'}(\boldsymbol{q}) l^\dagger_{sn_1k_1} l^\dagger_{s'n_2k_2} l_{s'n_3k_3} l_{sn_4k_4} \\ &\quad\times\langle\phi_{n_1k_1}|\boldsymbol{k}'_1\rangle\langle\boldsymbol{k}'_1 - \boldsymbol{q}|\phi_{n_4k_4}\rangle\langle\phi_{n_2k_2}|\boldsymbol{k}'_2\rangle\langle\boldsymbol{k}'_2 + \boldsymbol{q}|\phi_{n_3k_3}\rangle \\ &= \frac{1}{2\mathcal{V}}\sum_{ss'n_ik_i}\sum_{\boldsymbol{q}} V_{ss'}(\boldsymbol{q}) l^\dagger_{sn_1k_1} l^\dagger_{s'n_2k_2} l_{s'n_3k_3} l_{sn_4k_4} \\ &\quad\times\langle\phi_{n_1k_1}|e^{i\boldsymbol{q}\cdot\boldsymbol{r}}|\phi_{n_4k_4}\rangle\langle\phi_{n_2k_2}|e^{-i\boldsymbol{q}\cdot\boldsymbol{r}}|\phi_{n_3k_3}\rangle.\end{aligned} \tag{C8}$$

To get the last equality, we use the identity

$$\begin{aligned}\sum_{\boldsymbol{k}}|\boldsymbol{k}\rangle\langle\boldsymbol{k}-\boldsymbol{q}| &= \sum_{\boldsymbol{k}}\int d\boldsymbol{r}|\boldsymbol{k}\rangle\langle\boldsymbol{k}-\boldsymbol{q}|\boldsymbol{r}\rangle\langle\boldsymbol{r}| \\ &= \sum_{\boldsymbol{k}}\int d\boldsymbol{r}|\boldsymbol{k}\rangle e^{-i(\boldsymbol{k}-\boldsymbol{q})\cdot\boldsymbol{r}}\langle\boldsymbol{r}| \\ &= \sum_{\boldsymbol{k}}\int d\boldsymbol{r}|\boldsymbol{k}\rangle\langle\boldsymbol{k}|e^{i\boldsymbol{q}\cdot\boldsymbol{r}}|\boldsymbol{r}\rangle\langle\boldsymbol{r}| \\ &= e^{i\boldsymbol{q}\cdot\boldsymbol{r}}.\end{aligned} \tag{C9}$$

Notice that $\langle\phi_{n_2k_2}|e^{-i\boldsymbol{q}\cdot\boldsymbol{r}}|\phi_{n_3k_3}\rangle \propto \int dx\, e^{-i(k_2+q_x-k_3)x} \propto \delta_{k_3-k_2,q_x}$; Eq. (C8) is finally simplified to

$$H_I = \frac{1}{2\mathcal{V}}\sum_{ss'n_ik_i}\sum_{\boldsymbol{q}} V_{ss'}(\boldsymbol{q})e^{iq_y(k_1-k_2)\ell^2}\Lambda^*_{n_4n_1}(\boldsymbol{q})\Lambda_{n_2n_3}(\boldsymbol{q}) \times l^\dagger_{sn_1k_1+q_x/2}l^\dagger_{s'n_2k_2-q_x/2}l_{s'n_3k_2+q_x/2}l_{sn_4k_1-q_x/2}, \tag{C10}$$

where $\Lambda_{mn}(\boldsymbol{q})$ is the form factor for LLs,

$$\Lambda_{mn}(\boldsymbol{q}) \equiv \langle\phi_{mk-q_x/2}|e^{-i\boldsymbol{q}\cdot\boldsymbol{r}}|\phi_{nk+q_x/2}\rangle e^{ikq_y\ell^2} = \int dy\, e^{-iq_y\ell y}\psi_m(y+q_x\ell/2)\psi_n(y-q_x\ell/2). \tag{C11}$$

For $m \geqslant n$, $\Lambda_{mn}(\boldsymbol{q})$ is evaluated as [28]

$$\Lambda_{mn}(\boldsymbol{q}) = e^{-\frac{q^2\ell^2}{4}}\sqrt{\frac{m!}{n!}}\left(\frac{q_-\ell}{\sqrt{2}}\right)^{m-n}L_n^{(m-n)}\left(\frac{q^2\ell^2}{2}\right), \tag{C12}$$

where $q_- = q_x - iq_y$ and $L_n^{(\alpha)}(x)$ is the Laguerre polynomial; for $m < n$, $\Lambda_{mn}(\boldsymbol{q})$ can be determined by $\Lambda_{mn}(\boldsymbol{q}) = \Lambda^*_{nm}(-\boldsymbol{q})$.

## APPENDIX D: MEAN-FIELD CHANNELS IN MAGNETIC FIELD

As discussed in the main text, by requiring magnetic translation symmetry, the density matrix

$$\rho_{sn_1,s'n_2}(k_x) \equiv \langle l^\dagger_{s'n_2k_x}l_{sn_1k_x}\rangle - \delta_{ss'}\delta_{sh} \tag{D1}$$

is $k_x$ independent. Under Hartree-Fock approximation, the mean-field Fock Hamiltonian is decoupled as

$$H_F = -\frac{1}{2\mathcal{V}}\sum_{ss'n_ik}\sum_{\boldsymbol{q}} V_{ss'}(\boldsymbol{q})\Lambda^*_{n_4n_1}(\boldsymbol{q})\Lambda_{n_2n_3}(\boldsymbol{q}) \times [l^\dagger_{s'n_2k}l_{sn_4k}\rho_{s'n_3,sn_1} + l^\dagger_{sn_1k}l_{s'n_3k}\rho_{sn_4,s'n_2}]. \tag{D2}$$

According to Eq. (C12), we have $\Lambda_{mn}(\boldsymbol{q}) \propto e^{-i(m-n)\theta_{\boldsymbol{q}}}$. Thus, the $\boldsymbol{q}$ summation in Eq. (D2) is nonzero only when $n_4 - n_1 = n_2 - n_3$. It is convenient to define $M = n_3 - n_1 = n_2 - n_4$, which labels independent condensation channels. For a condensation channel labeled by $M$, the only surviving density matrix elements are $\rho_{s'M+n,sn}$ and $\rho_{sn,s'n+M}$.

We argue that the index $M$ is just the angular momentum of the exciton condensation. In the absence of a magnetic field, the density matrix for the exciton condensation of angular momentum $M$ takes the form

$$\rho_{ehk} \sim k_+^M f(k^2), \tag{D3}$$

where $k_+ = k_x + ik_y$ and $f$ is some analytic function. After Peierls substitution and projecting to the LL basis, we have

$$\begin{aligned}&\langle e,\phi_{nk_x}|\rho_\Pi|h,\phi_{mk'_x}\rangle \\ &\sim \langle\phi_{nk_x}|\Pi_+^M f(\Pi^2/\hbar^2)|\phi_{mk'_x}\rangle \\ &\sim \langle\phi_{nk_x}|\Pi_+^M|\phi_{mk'_x}\rangle f((2m+1)eB/\hbar) \\ &\sim \delta_{n,m+M}\delta_{k_xk'_x}.\end{aligned} \tag{D4}$$

Due to Hermiticity, $\langle h,\phi_{nk_x}|\rho_\Pi|e,\phi_{mk'_x}\rangle \sim \delta_{n+M,m}\delta_{k_xk'_x}$. Thus, for exciton condensation of angular momentum $M$, the only surviving EI order parameters under LL basis are $\rho_{en+M,hn}$ and $\rho_{hn,en+M}$.

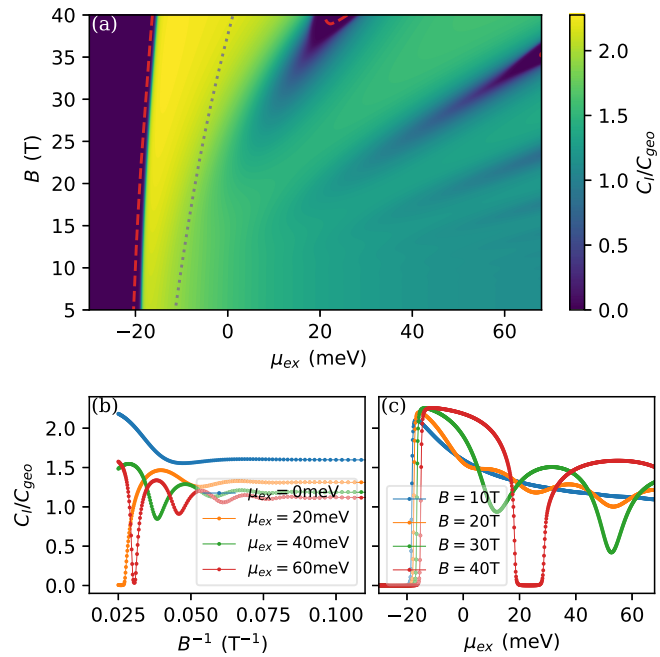


FIG. 6. The same quantities as in Fig. 4, expect that a finite tunneling strength $t = 0.01$ meV is used.

## APPENDIX E: CAPACITANCE OSCILLATION AT FINITE INTERLAYER TUNNELING

With a finite tunneling strength $t = 0.01$ meV, the same quantities as in Fig. 4 are calculated and shown in Fig. 6. At this time, there is no phase transition since the off-diagonal part of the density matrix $\rho_{\text{eh}}$ never goes to zero due to the persistent single-particle tunneling $t$. And the red solid lines which mark the phase boundaries in Fig. 4(a) are replaced by the red dashed lines (determined by $\max_n|\rho_{n,eh}| = 0.01$) in Fig. 6(a), which could be used to indicate the crossover. It is easily seen from Fig. 6 that the main results of the single-particle tunneling are to smooth the curves of the interlayer capacitance just like in the case without magnetic field.

Using $B = 15$ T as an example, oscillations of $\Delta C_I$ versus $n_{\text{ex}}$ at different tunneling strengths are plotted in Fig. 7, and

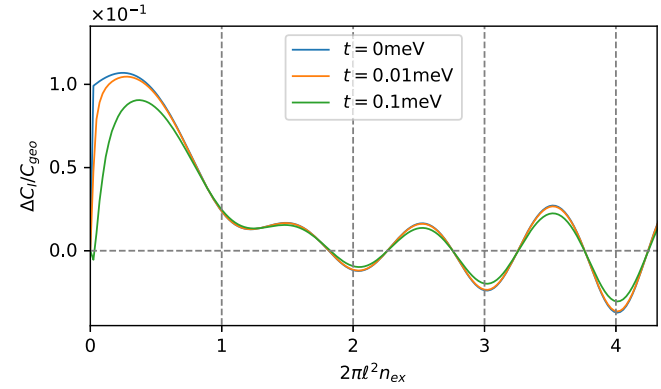


FIG. 7. Oscillations of $\Delta C_I$ versus $n_{\text{ex}}$ for different tunneling strengths. The magnetic field strength is taken as $B = 15$ T.

the oscillation amplitudes get smaller when the interlayer tunneling is included.

## APPENDIX F: EFFECT OF SINGLE-PARTICLE HYBRIDIZATION ON THE INTERLAYER CAPACITANCE

Let us assume a nonzero tunneling strength $t \neq 0$ and ignore the exchange part of the interaction, which accounts for the exciton condensation. Then the charge density per layer is calculated as

$$n_{\rm ex} = \frac{1}{4\pi\ell^2}\sum_n \left[1 - \frac{\hbar\omega^*(2n+1) - \tilde{\mu}_{\rm ex}}{\sqrt{[\hbar\omega^*(2n+1) - \tilde{\mu}_{\rm ex}]^2 + 4t^2}}\right], \tag{F1}$$

where $\omega^* = (\omega_e + \omega_h)/2$ and $\tilde{\mu}_{\rm ex} = \mu_{\rm ex} - e^2 n_{\rm ex}/C_{\rm geo}$ is the renormalized "exciton chemical potential" from interlayer geometry electrostatic energy. By definition, the interlayer capacitance should be calculated as

$$C_I \equiv e^2\frac{\partial n_{\rm ex}}{\partial \mu_{\rm ex}} = e^2\frac{\partial n_{\rm ex}}{\partial \tilde{\mu}_{\rm ex}}\frac{\partial \tilde{\mu}_{\rm ex}}{\partial \mu_{\rm ex}} = e^2\frac{\partial n_{\rm ex}}{\partial \tilde{\mu}_{\rm ex}}\left(1 - \frac{C_I}{C_{\rm geo}}\right). \tag{F2}$$

Denoting $\tilde{C}_I = e^2\partial n_{\rm ex}/\partial\tilde{\mu}_{\rm ex}$, the interlayer capacitance is solved as $C_I = (\tilde{C}_I^{-1} + C_{\rm geo}^{-1})^{-1}$. It is easily verified that

$$\tilde{C}_I = \frac{e^2}{4\pi\ell^2}\sum_n \frac{4t^2}{\{[\hbar\omega^*(2n+1) - \tilde{\mu}_{\rm ex}]^2 + 4t^2\}^{3/2}} > 0 \tag{F3}$$

as long as the hybridization strength $t$ is nonzero, and the interlayer capacitance must satisfy $0 < C_I < C_{\rm geo}$.


[1] L. V. Butov, A. Zrenner, G. Abstreiter, G. Böhm, and G. Weimann, Condensation of indirect excitons in coupled AlAs/GaAs quantum wells, Phys. Rev. Lett. **73**, 304 (1994).

[2] X. Zhu, P. B. Littlewood, M. S. Hybertsen, and T. M. Rice, Exciton condensate in semiconductor quantum well structures, Phys. Rev. Lett. **74**, 1633 (1995).

[3] P. B. Littlewood and X. Zhu, Possibilities for exciton condensation in semiconductor quantum-well structures, Phys. Scr. **1996**, 56 (1996).

[4] L. V. Butov, Exciton condensation in coupled quantum wells, Solid State Commun. **127**, 89 (2003).

[5] P. B. Littlewood, P. R. Eastham, J. M. J. Keeling, F. M. Marchetti, B. D. Simons, and M. H. Szymanska, Models of coherent exciton condensation, J. Phys.: Condens. Matter **16**, S3597 (2004).

[6] H. Min, R. Bistritzer, J.-J. Su, and A. H. MacDonald, Room-temperature superfluidity in graphene bilayers, Phys. Rev. B **78**, 121401(R) (2008).

[7] M. M. Fogler, L. V. Butov, and K. S. Novoselov, High-temperature superfluidity with indirect excitons in van der Waals heterostructures, Nat. Commun. **5**, 4555 (2014).

[8] F.-C. Wu, F. Xue, and A. H. MacDonald, Theory of two-dimensional spatially indirect equilibrium exciton condensates, Phys. Rev. B **92**, 165121 (2015).

[9] M. Xie and A. H. MacDonald, Electrical reservoirs for Bilayer excitons, Phys. Rev. Lett. **121**, 067702 (2018).

[10] M. Trushin, Interlayer excitonic insulator in two-dimensional double-layer semiconductor junctions: An explicitly solvable model, Phys. Rev. B **106**, 125311 (2022).

[11] I. Amelio, N. D. Drummond, E. Demler, R. Schmidt, and A. Imamoglu, Polaron spectroscopy of a bilayer excitonic insulator, Phys. Rev. B **107**, 155303 (2023).

[12] L. Du, X. Li, W. Lou, G. Sullivan, K. Chang, J. Kono, and R.-R. Du, Evidence for a topological excitonic insulator in InAs/GaSb bilayers, Nat. Commun. **8**, 1971 (2017).

[13] Z. Wang, Y.-H. Chiu, K. Honz, K. F. Mak, and J. Shan, Electrical tuning of interlayer exciton gases in $WSe_2$ Bilayers, Nano Lett. **18**, 137 (2018).

[14] Z. Wang, D. A. Rhodes, K. Watanabe, T. Taniguchi, J. C. Hone, J. Shan, and K. F. Mak, Evidence of high-temperature exciton condensation in two-dimensional atomic double layers, Nature (London) **574**, 76 (2019).

[15] L. Ma, P. X. Nguyen, Z. Wang, Y. Zeng, K. Watanabe, T. Taniguchi, A. H. MacDonald, K. F. Mak, and J. Shan, Strongly correlated excitonic insulator in atomic double layers, Nature (London) **598**, 585 (2021).

[16] P. X. Nguyen, L. Ma, R. Chaturvedi, K. Watanabe, T. Taniguchi, J. Shan, and K. F. Mak, Perfect Coulomb drag in a dipolar excitonic insulator, arXiv:2309.14940.

[17] G.-B. Liu, W.-Y. Shan, Y. Yao, W. Yao, and D. Xiao, Three-band tight-binding model for monolayers of group-VIB transition metal dichalcogenides, Phys. Rev. B **88**, 085433 (2013).

[18] D. Jérome, T. M. Rice, and W. Kohn, Excitonic insulator, Phys. Rev. **158**, 462 (1967).

[19] J. P. Eisenstein and A. H. MacDonald, Bose–Einstein condensation of excitons in bilayer electron systems, Nature (London) **432**, 691 (2004).

[20] D. Nandi, A. D. K. Finck, J. P. Eisenstein, L. N. Pfeiffer, and K. W. West, Exciton condensation and perfect Coulomb drag, Nature (London) **488**, 481 (2012).

[21] Q. Zhu, M. W.-Y. Tu, Q. Tong, and W. Yao, Gate tuning from exciton superfluid to quantum anomalous Hall in van der Waals heterobilayer, Sci. Adv. **5**, eaau6120 (2019).

[22] Q. Tong, H. Yu, Q. Zhu, Y. Wang, X. Xu, and W. Yao, Topological mosaics in moiré superlattices of van der Waals heterobilayers, Nat. Phys. **13**, 356 (2017).

[23] Y. Yoon, Z. Zhang, R. Qi, A. Y. Joe, R. Sailus, K. Watanabe, T. Taniguchi, S. Tongay, and F. Wang, Charge transfer dynamics in $MoSe_2$/hBN/$WSe_2$ heterostructures, Nano Lett. **22**, 10140 (2022).

[24] A. Zee, Quantum Hall fluids, Field Theory, Topology and Condensed Matter Physics, in *Proceedings of the Ninth Chris Engelbrecht Summer School in Theoretical Physics Held at Storms River Mouth, Tsitsikamma National Park, South Africa, 17–28 January 1994* (Springer, Berlin, Heidelberg, Berlin, Heidelberg, 2007), pp. 99–153.

[25] Y. Zeng and A. H. MacDonald, Electrically controlled two-dimensional electron-hole fluids, Phys. Rev. B **102**, 085154 (2020).

[26] L. D. Hallam, J. Weis, and P. A. Maksym, Screening of the electron-electron interaction by gate electrodes in semiconductor quantum dots, Phys. Rev. B **53**, 1452 (1996).
[27] Y.-P. Shim and A. H. MacDonald, Spin-orbit interactions in bilayer exciton-condensate ferromagnets, Phys. Rev. B **79**, 235329 (2009).
[28] A. H. MacDonald, Influence of Landau-level mixing on the charge-density-wave state of a two-dimensional electron gas in a strong magnetic field, Phys. Rev. B **30**, 4392 (1984).
[29] D. Xiao, G.-B. Liu, W. Feng, X. Xu, and W. Yao, Coupled spin and valley physics in monolayers of $MoS_2$ and other group-VI dichalcogenides, Phys. Rev. Lett. **108**, 196802 (2012).
[30] B. Zou, Y. Zeng, A. H. MacDonald, and A. Strashko, Electrical control of two-dimensional electron-hole fluids in the quantum Hall regime, arXiv:2309.04600.
[31] A. Kormányos, G. Burkard, M. Gmitra, J. Fabian, V. Zólyomi, N. D. Drummond, and V. Fal'ko, K·p theory for two-dimensional transition metal dichalcogenide semiconductors, 2D Mater. **2**, 022001 (2015).
[32] Y. Cai, L. Zhang, Q. Zeng, L. Cheng, and Y. Xu, Infrared reflectance spectrum of BN calculated from first principles, Solid State Commun. **141**, 262 (2007).
[33] A. Filinov, N. V. Prokof'ev, and M. Bonitz, Berezinskii-Kosterlitz-Thouless transition in two-dimensional dipole systems, Phys. Rev. Lett. **105**, 070401 (2010).
[34] D. Shoenberg, *Magnetic Oscillations in Metals* (Cambridge University Press, Cambridge, 2009).
[35] J. Knolle and N. R. Cooper, Quantum oscillations without a Fermi surface and the anomalous de Haas–van Alphen effect, Phys. Rev. Lett. **115**, 146401 (2015).
[36] L. Zhang, X.-Y. Song, and F. Wang, Quantum oscillation in narrow-gap topological insulators, Phys. Rev. Lett. **116**, 046404 (2016).
[37] N. P. Ong, Quantum oscillations in an insulator, Science **362**, 32 (2018).
[38] Z. Xiang, Y. Kasahara, T. Asaba, B. Lawson, C. Tinsman, L. Chen, K. Sugimoto, S. Kawaguchi, Y. Sato, G. Li, S. Yao, Y. L. Chen, F. Iga, J. Singleton, Y. Matsuda, and L. Li, Quantum oscillations of electrical resistivity in an insulator, Science **362**, 65 (2018).
[39] A. Panda, S. Banerjee, and M. Randeria, Quantum oscillations in the magnetization and density of states of insulators, Proc. Natl. Acad. Sci. USA **119**, e2208373119 (2022).
[40] K. Suzuki, K. Takashina, S. Miyashita, and Y. Hirayama, Landau-level hybridization and the quantum Hall effect in InAs/GaSb electron-hole systems, Phys. Rev. Lett. **93**, 016803 (2004).
[41] B. S. Tan, Y.-T. Hsu, B. Zeng, M. C. Hatnean, N. Harrison, Z. Zhu, M. Hartstein, M. Kiourlappou, A. Srivastava, M. D. Johannes, T. P. Murphy, J.-H. Park, L. Balicas, G. G. Lonzarich, G. Balakrishnan, and S. E. Sebastian, Unconventional Fermi surface in an insulating state, Science **349**, 287 (2015).
[42] Z. Han, T. Li, L. Zhang, G. Sullivan, and R.-R. Du, Anomalous conductance oscillations in the hybridization gap of InAs/GaSb quantum wells, Phys. Rev. Lett. **123**, 126803 (2019).
[43] D. Xiao, C.-X. Liu, N. Samarth, and L.-H. Hu, Anomalous quantum oscillations of interacting electron-hole gases in inverted type-II InAs/GaSb quantum wells, Phys. Rev. Lett. **122**, 186802 (2019).
[44] E. W. Fenton, Excitonic insulator in a magnetic field, Phys. Rev. **170**, 816 (1968).
[45] H. Fukuyama, T. Tsuzuki, and S. Nakajima, Dimensionality of density fluctuations and the excitonic phase of electron-hole systems in strong magnetic fields, J. Phys. Soc. Jpn. **39**, 1439 (1975).
[46] T. Nagai and T. Tsuzuki, Excitonic phase in a strong magnetic field. I. Phase diagram, J. Low Temp. Phys. **25**, 9 (1976).
[47] Y. Kuramoto and M. Morimoto, Electron-hole pair condensation and liquefaction in strong magnetic fields, J. Phys. Soc. Jpn. **44**, 1759 (1978).
[48] Y. Shao and X. Dai, Electrical breakdown of excitonic insulator, arXiv:2302.07543.
[49] E. Brown, Bloch electrons in a uniform magnetic field, Phys. Rev. **133**, A1038 (1964).